PERGAMON

International Journal of Heat and Mass Transfer 46 (2003) 791–808

International Journal of
HEAT and MASS TRANSFER

www.elsevier.com/locate/ijhmt

Three-dimensional convective cooling in a vertical channel with flush-mounted heat sources

H. Gunes [a,*], A. Liakopoulos [b,1]

[a] Department of Mechanical Engineering, Istanbul Technical University, Gumussuyu, 80191 Istanbul, Turkey
[b] Department of Mechanical Engineering and Mechanics, Lehigh University, Bethlehem, PA 18015-3085, USA

Received 12 November 2000; received in revised form 26 August 2002

Abstract

Three-dimensional free convection in a vertical channel with spatially periodic, flush-mounted heat sources is investigated by a spectral element method. All numerical solutions are obtained using a time-accurate finite-difference integration scheme capable of capturing temporal instabilities that spontaneously appear at large values of Grashof number, Gr. In addition, the leading order approximation of the 3-D solution for small Gr is derived and compared with the numerical solutions. The agreement is excellent for sufficiently small Gr.

Computations are carried out for a Boussinesq fluid, Prandtl number, $Pr = 0.71$, non-dimensional reference temperature, $\Theta_b^* = 0.12$ and values of Grashof number in the range $0.1 \leqslant Gr \leqslant 5 \times 10^4$. For given aspect ratios, and for sufficiently small values of Grashof number, the solution evolves to a unique, time-independent state that exhibits the maximum symmetry consistent with the boundary conditions. At $Gr^* \simeq 28{,}000$, self-sustained oscillations appear spontaneously in the flow and thermal fields. For time-dependent solutions ($Gr \geqslant Gr^*$) the symmetry of the flow and temperature fields breaks down.

Temperature and velocity distributions as well as maximum temperature, maximum velocity and local Nusselt number distributions are presented for the values of Grashof number studied. For time-dependent flows, instantaneous as well as averaged-in-time solutions are discussed.

1. Introduction

Natural convection is an effective mode of heat transfer for both air and liquid cooling when surface heat fluxes are relatively small. Because of its simplicity and reliability, it has important advantages over other cooling modes. In addition, if thermal control using the natural convection cooling is adopted, it eliminates the fan or pump and provides a noise- and vibration-free environment [1]. Consequently, communications switching devices, avionics packages, electronic test equipment, consumer electronics, and low-end computer packages are often air-cooled by natural convection [2,3]. Modeling of typical configurations encountered in second level electronics packaging, lead to the consideration of free convection cooling in tall enclosures or vertical channels.

The vast majority of studies on natural convection in cavities and channels deals with 2-D geometries, mostly cavities formed by two parallel vertical surfaces held at different uniform temperatures or uniform heat fluxes and, in the case of cavities, with adiabatic or constant-temperature top and bottom walls. Although these studies treat an important class of problems with significant practical applications, complexities present in many real problems are neglected by ignoring the third dimension [4].

Liakopoulos et al. [5] and Huang and Liakopoulos [6] investigated numerically 2-D thermally driven convective flows in tall cavities and vertical channels for $Pr = 0.71$ and a wide range of values of Grashof number,

---

[*] Corresponding author. Tel.: +90-212-293-1300x2707; fax: +90-212-245-0795.
E-mail address: guneshasa@itu.edu.tr (H. Gunes).

[1] Present address: Department of Civil Engineering, University of Thessaly, Pedion Areos, 383 34 Volos, Greece.

0017-9310/03/$ - see front matter © 2002 Elsevier Science Ltd. All rights reserved.
PII: S0017-9310(02)00351-4

Nomenclature

A_{cy}, A_{cz}	heat source aspect ratios, l_{cy}/l, l_{cz}/l
A_{sy}, A_{sz}	heat source spacing aspect ratios, l_{sy}/l, l_{sz}/l
A_y	height aspect ratio of the computational domain, h/l
A_z	depth aspect ratio of the computational domain, b/l
b	computational domain depth
c_p	specific heat
g	gravitational acceleration
Gr	Grashof number, $\beta g q'' l^4/\nu^2 k$
h	computational domain height
k	thermal conductivity of the fluid
K	number of macro-elements
l	channel width
l_{cy}, l_{cz}	dimensions of heat source
l_{sy}, l_{sz}	distances between heat sources
N	order of interpolants + 1
Nu	local Nusselt number
$\overline{Nu}$	average Nusselt number
p	pressure
P	non-dimensional pressure, $(l^2/\rho_0\alpha^2)p$
Pr	Prandtl number, ν/α
q''	dissipated heat flux
Q	dimensionless volume flow rate
Ra	Rayleigh number, $\beta g q'' l^4/\nu\alpha k$
t^*	dimensionless time
t	time
T	dimensional temperature
u, v, w	dimensional velocity components
U, V, W	non-dimensional velocity components
$\vec{V}$	velocity vector
x, y, z	Cartesian coordinates
X, Y, Z	non-dimensional Cartesian coordinates

Greek symbols

α	thermal diffusivity
β	thermal expansion coefficient
$\partial\Omega_{\mathrm{A}}$	adiabatic surface
$\partial\Omega_{\mathrm{C}}$	constant heat flux surface
$\partial\Omega_{\mathrm{T}}$	constant temperature surface
Δt	time integration step
Θ	non-dimensional temperature, $(k/q''l) \times (T - T_{\mathrm{b}})$
μ	dynamic viscosity
ν	kinematic viscosity
ρ	density

Subscripts

an	analytical value
b	reference value
C	chip carrier
l	left wall
max	maximum value in the computational domain
num	numerical value
r	right wall

Gr. The study presented in this paper is the 3-D generalization of the 2-D configuration considered in the previous papers. Keyhani et al. [7] performed experiments on natural convection in a ethylene glycol-filled ($Pr = 150$) vertical cavity with discrete heat sources. A cavity of aspect ratio $A_y = 16.5$ was formed with 11 alternately unheated and flush-heated sections of equal height on one of the vertical wall and the other vertical wall was kept isothermal. The horizontal walls were adiabatic. They found that discrete flush-mounted heaters resulted in local Nusselt numbers similar to those reported by Park and Bergles [8], who investigated the effect of heater width on natural convection, for a single wide flush-mounted heater on a vertical plate. Joshi and Knight [9] studied natural convection from a column of heat sources flush mounted on one wall of a vertical channel immersed in water. They investigated the effect of heater and channel spacing on heat transfer. While there are many two-dimensional simulations in the literature few three-dimensional numerical studies have been performed. Kuhn and Oosthuizen [10] reported an analysis of 3-D, transient, natural convection flow in a rectangular enclosure with localized heating. They found that three-dimensional flow increased the local heat transfer coefficient at the edges of the element resulting in a higher average Nusselt number than the corresponding 2-D flow. However, the difference decreased as the Rayleigh number was increased, being nearly the same at $Ra = 10^5$. Their results for two spanwise, in-line, flush-mounted, symmetrically placed heaters indicate that the distance between the elements has little effect on the mean heat transfer rate variation but has a considerable effect on the local *Nu* number distribution. Recently, three-dimensional, steady, natural convection from a discrete flush-mounted rectangular heat source on the bottom of a horizontal enclosure is studied numerically [11]. Lee [12] performed combined numerical and theoretical analyses to investigate the natural convection heat and mass transfer in vertical ducts. The literature on free convection in cavities and channels with protruding heat sources has been reviewed by Gunes and Liakopoulos [13].

In the present study, three-dimensional buoyancy-driven flow and heat transfer generated by periodically spaced heat sources of uniform heat flux, flush mounted on the left vertical wall of a vertical channel are exam-

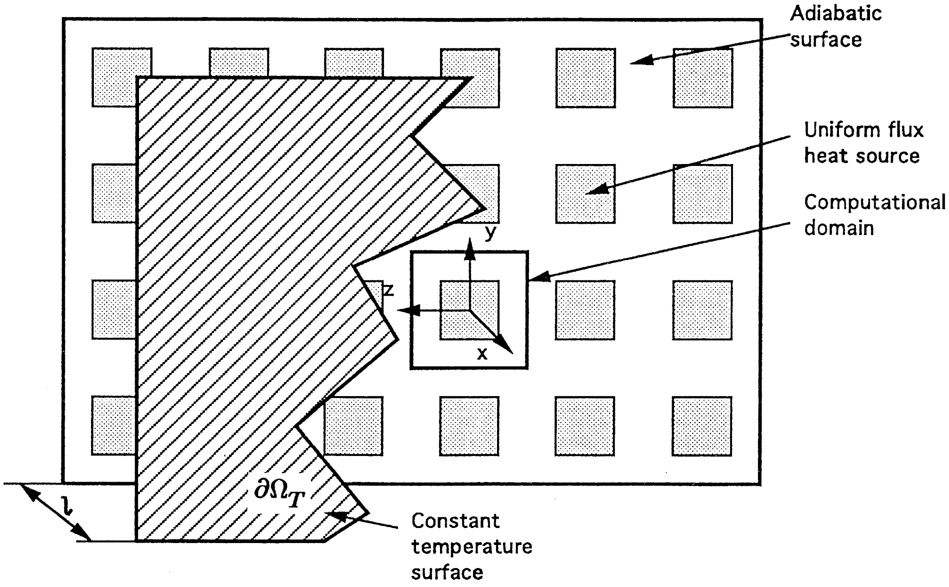

Fig. 1. Problem configuration.

ined. The right vertical wall is kept isothermal. The geometry is shown in Fig. 1. Chip carriers are modeled as flush-mounted heat sources with constant heat flux. A detailed description of the computational domain and the associated thermal boundary conditions are given in Fig. 2. Periodic boundary conditions are imposed on both velocity and temperature fields, i.e., velocity and temperature in the computational domain inlet ($y = -h/2$ plane) are the same as in the computational domain exit ($y = h/2$ plane) as well as at the vertical planes of $z = -b/2$ and $z = b/2$. All simulations performed are time accurate. If a steady (time-independent) solution exists it is found as the steady-state solution of an appropriate initial boundary value problem, after all transients die out, i.e., in the limit $t \to \infty$.

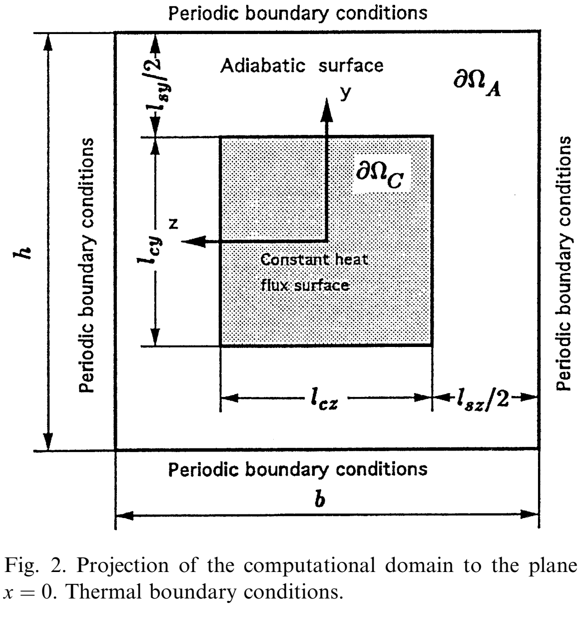

Fig. 2. Projection of the computational domain to the plane $x = 0$. Thermal boundary conditions.

2. Mathematical model

In this study, 3-D, laminar, possibly time-dependent natural convection flow of a *Boussinesq* fluid is considered. Neglecting viscous dissipation and energy generation in the fluid domain, the governing partial differential equations, conservation of mass, momentum and energy, can be written in dimensionless form as follows:

$$\frac{\partial U}{\partial X} + \frac{\partial V}{\partial Y} + \frac{\partial W}{\partial Z} = 0, \tag{1}$$

$$\frac{\partial U}{\partial t^*} + U\frac{\partial U}{\partial X} + V\frac{\partial U}{\partial Y} + W\frac{\partial U}{\partial Z} = -\frac{\partial P}{\partial X} + Pr\left[\frac{\partial^2 U}{\partial X^2} + \frac{\partial^2 U}{\partial Y^2} + \frac{\partial^2 U}{\partial Z^2}\right], \tag{2}$$

$$\frac{\partial V}{\partial t^*} + U\frac{\partial V}{\partial X} + V\frac{\partial V}{\partial Y} + W\frac{\partial V}{\partial Z} = -\frac{\partial P}{\partial Y} + Pr\,Ra\,\Theta + Pr\left[\frac{\partial^2 V}{\partial X^2} + \frac{\partial^2 V}{\partial Y^2} + \frac{\partial^2 V}{\partial Z^2}\right], \tag{3}$$

$$\frac{\partial W}{\partial t^*} + U\frac{\partial W}{\partial X} + V\frac{\partial W}{\partial Y} + W\frac{\partial W}{\partial Z} = -\frac{\partial P}{\partial Z} + Pr\left[\frac{\partial^2 W}{\partial X^2} + \frac{\partial^2 W}{\partial Y^2} + \frac{\partial^2 W}{\partial Z^2}\right], \tag{4}$$

$$\frac{\partial \Theta}{\partial t^*} + U\frac{\partial \Theta}{\partial X} + V\frac{\partial \Theta}{\partial Y} + W\frac{\partial \Theta}{\partial Z} = \left[\frac{\partial^2 \Theta}{\partial X^2} + \frac{\partial^2 \Theta}{\partial Y^2} + \frac{\partial^2 \Theta}{\partial Z^2}\right]. \tag{5}$$

The independent and dependent variables have been non-dimensionalized using

$$(X, Y, Z) = \frac{1}{l}(x, y, z), \quad t^* = \frac{\alpha}{l^2}t, \tag{6}$$

$$(U, V, W) = \frac{l}{\alpha}(u, v, w), \quad P = \frac{l^2}{\rho_0 \alpha^2}p, \quad \Theta = \frac{k}{q'' l}(T - T_\mathrm{b}). \tag{7}$$

In general, lower case letters denote dimensional variables. However, note that the dimensional temperature is denoted by T and the dimensionless time is denoted by t^*. In the above, (x, y, z) and (u, v, w) denote the Cartesian coordinates and velocity components, respectively, p is the pressure relative to the background hydrostatic distribution, l is the width of the vertical channel (see Fig. 1), k is the thermal conductivity of the fluid, α is the thermal diffusivity, ν is the kinematic viscosity, β is the thermal expansion coefficient, g is the gravitational acceleration, ρ_0 is the reference density, T_b is the reference temperature, q'' denotes the uniform input heat flux of the heat sources, $Pr = \nu/\alpha$ denotes the Prandtl number and $Ra = \beta g q'' l^4/\nu\alpha k$ denotes the Rayleigh number.

To describe the computational domain we introduce aspect ratios $A_z = b/l$ and $A_y = h/l$ where l denotes the width of the vertical channel. The heat source aspect ratios are defined as $A_{cz} = l_{cz}/l$ and $A_{cy} = l_{cy}/l$ and the chip spacing aspect ratios are $A_{sy} = l_{sy}/l$ and $A_{sz} = l_{sz}/l$, as shown in Fig. 2.

The associated boundary conditions for the configuration considered in this paper are:

$$\vec{V}(X, Y, Z, t^*) = 0 \quad \text{at all solid walls}, \tag{8}$$

$$\vec{V}(X, -A_y/2, Z, t^*) = \vec{V}(X, A_y/2, Z, t^*), \tag{9a}$$

$$\vec{V}(X, Y, -A_z/2, t^*) = \vec{V}(X, Y, A_z/2, t^*), \tag{9b}$$

$$\frac{\partial \Theta}{\partial X} = \begin{cases} -1, & \text{on } \partial\Omega_\mathrm{C}, \\ 0, & \text{on } \partial\Omega_\mathrm{A}, \end{cases} \tag{10}$$

$$\Theta = \frac{k}{q'' l}(T_\mathrm{C} - T_\mathrm{b}) = -\Theta_\mathrm{b}^* \quad \text{on } \partial\Omega_\mathrm{T}, \tag{11}$$

$$\Theta(X, -A_y/2, Z, t^*) = \Theta(X, A_y/2, Z, t^*), \tag{12a}$$

$$\Theta(X, Y, -A_z/2, t^*) = \Theta(X, Y, A_z/2, t^*). \tag{12b}$$

3. Method of solution

The governing equations (1)–(5) with the appropriate boundary conditions are solved by a spectral element method [14]. Spectral element methods are high-order weighted-residual techniques. Their success is mainly due to their ability to represent relatively complex geometries while preserving the good resolution properties of the spectral methods [15]. In standard finite element methods (h-type), convergence is reached by increasing the number of elements, K, in the computational domain leading to an algebraic rate of error decrease. On the other hand, in p-type finite element methods convergence is reached by increasing the order of polynomials used as basis functions, leading to faster error decay for smooth solutions. Becker et al. [16] notes that the p-type finite element method achieves better convergence rates (energy norm versus number of degrees of freedom) than the h-method for smooth solutions. In the presence of singularities, optimal convergence rates are achieved by a combination of the h- and p-methods. In h–p methods, one obtains higher efficiencies by varying both macro-elements (grid size h) and the polynomial degree (p).

In the spectral element used in our simulations, the computational domain is subdivided into K non-overlapping macro-elements. Within each element, a local mesh is constructed for the velocity and temperature fields corresponding to $N \times N \times N$ Gauss–Lobatto–Legendre collocation points. Within each element the velocity and temperature fields are expanded in terms of $(N-1)$th order tensor-product Lagrangian interpolants through the Gauss–Lobatto–Legendre collocation points, while the pressure field is approximated in terms of the $(N-2)$th order Lagrangian interpolants through

Table 1
Comparison of numerical and analytical solutions ($Pr = 0.71$, $A_{cy} = A_{cz} = 2$, $A_y = A_z = 4$, $\Theta_\mathrm{b}^* = 0.125$)

Gr	$[\Theta_{\max}]_{\mathrm{num}}$	$[\Theta_{\max}]_{\mathrm{an}}$	Rel. Er. (%)	$[V_{\max}]_{\mathrm{num}}$	$[V_{\max}]_{\mathrm{an}}$	Rel. Er. (%)
0.1	0.6037	0.6036	0.02	9.1×10^{-4}	9.1×10^{-4}	0.0
1	0.6037	0.6036	0.02	9.1×10^{-3}	9.1×10^{-3}	0.0
100	0.6015	0.6036	0.35	0.9058	0.9100	0.46
200	0.5991	0.6036	0.75	1.8006	1.8200	1.1
500	0.5769	0.6036	4.4	4.3629	4.5500	4.1

Table 2
Comparison of numerical and analytical solutions ($Pr = 0.71$, $A_{cy} = A_{cz} = 2$, $A_y = A_z = 4$, $\Theta_b^* = 0.125$)

Gr	$[U_{\max}]_{\text{num}}$	$[U_{\max}]_{\text{an}}$	Rel. Er. (%)	$[W_{\max}]_{\text{num}}$	$[W_{\max}]_{\text{an}}$	Rel. Er. (%)
0.1	8.8×10^{-5}	8.8×10^{-5}	0.0	1.8×10^{-4}	1.8×10^{-4}	0.0
1	8.9×10^{-4}	8.8×10^{-4}	1.1	1.8×10^{-3}	1.8×10^{-3}	0.0
100	0.08923	0.08823	1.1	0.18209	0.18185	0.13
200	0.17964	0.17646	1.8	0.35617	0.36370	2.1
500	0.39543	0.44115	11.6	0.78210	0.90925	16.3

Table 3
Comparison of numerical and analytical solutions ($Pr = 0.71$, $A_{cy} = A_{cz} = 2$, $A_y = A_z = 4$, $\Theta_b^* = 0.125$)

Gr	$[P_{\max}]_{\text{num}}$	$[P_{\max}]_{\text{an}}$	Rel. Er. (%)
0.1	0.00379	0.00375	1.0
1	0.03790	0.03751	1.0
100	3.7735	3.7514	0.6
200	7.3553	7.5028	2.0
500	15.8537	18.757	18.3

the Gauss–Legendre collocation points. Spatial convergence is obtained by increasing N or K, or both.

Integration in time is performed using conventional finite difference techniques. The non-linear convection terms in Eqs. (2)–(5) and body-force term in Eq. (3) are integrated explicitly in time using a third-order Adams–Bashforth scheme, whereas the diffusion terms, the pressure gradient and the continuity equation (1) are treated *implicitly* using a sth-order backward-differentiation formula. Numerical results presented in this paper have been obtained with $s = 1$ or 2. The explicit treatment of the non-linear terms results in a limitation on the maximum allowable time step, Δt, i.e., a Courant condition should be satisfied in order to ensure numerical stability.

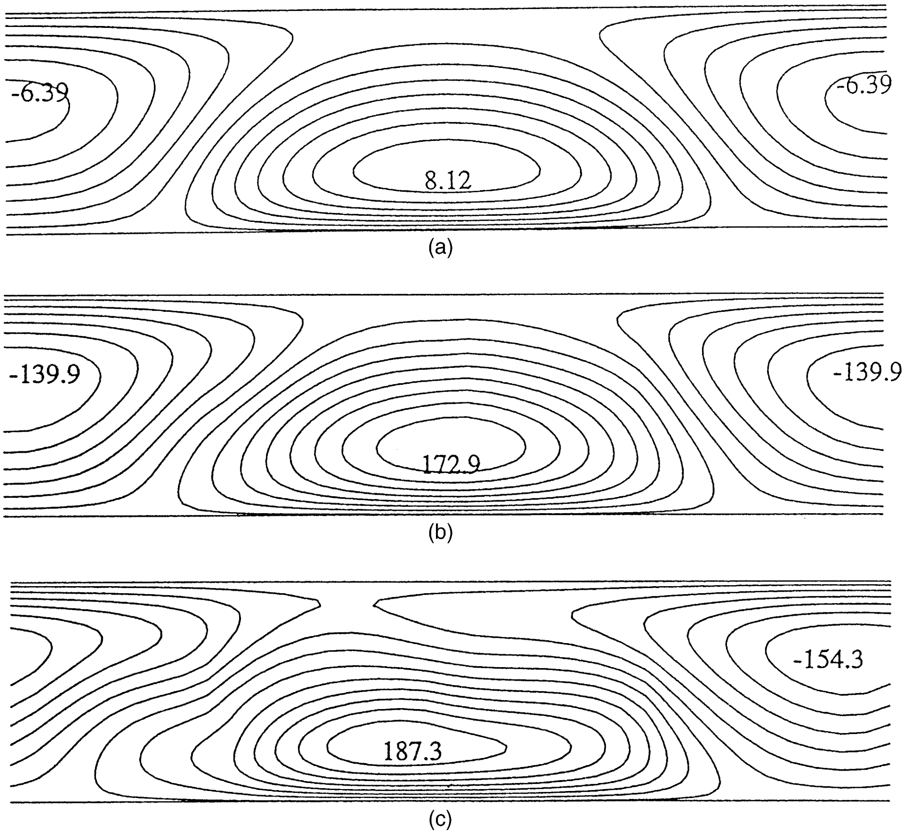

Fig. 3. Vertical velocity component contours at $Y = 0$. (a) $Gr = 1000$, (b) $Gr = 30{,}000$, (c) $Gr = 50{,}000$.

Implementation of the numerical methods described above is based on Nekton [17], a computer code, developed by Patera and his co-workers, for the simulation of steady and unsteady incompressible fluid flow, heat and mass transfer. At high values of Grashof number computations are performed using a standard time-split formulation [18]. At low Grashof numbers ($Gr \leqslant 100$), solutions are computed using Uzawa's algorithm. This eliminates the splitting errors that can arise at speeds characteristic of small Grashof number flows. In our numerical simulations we have typically used $K = 128$ elements and $N = 5$, which provides excellent accuracy for small and moderate values of Gr. For high values of Grashof number, solutions with

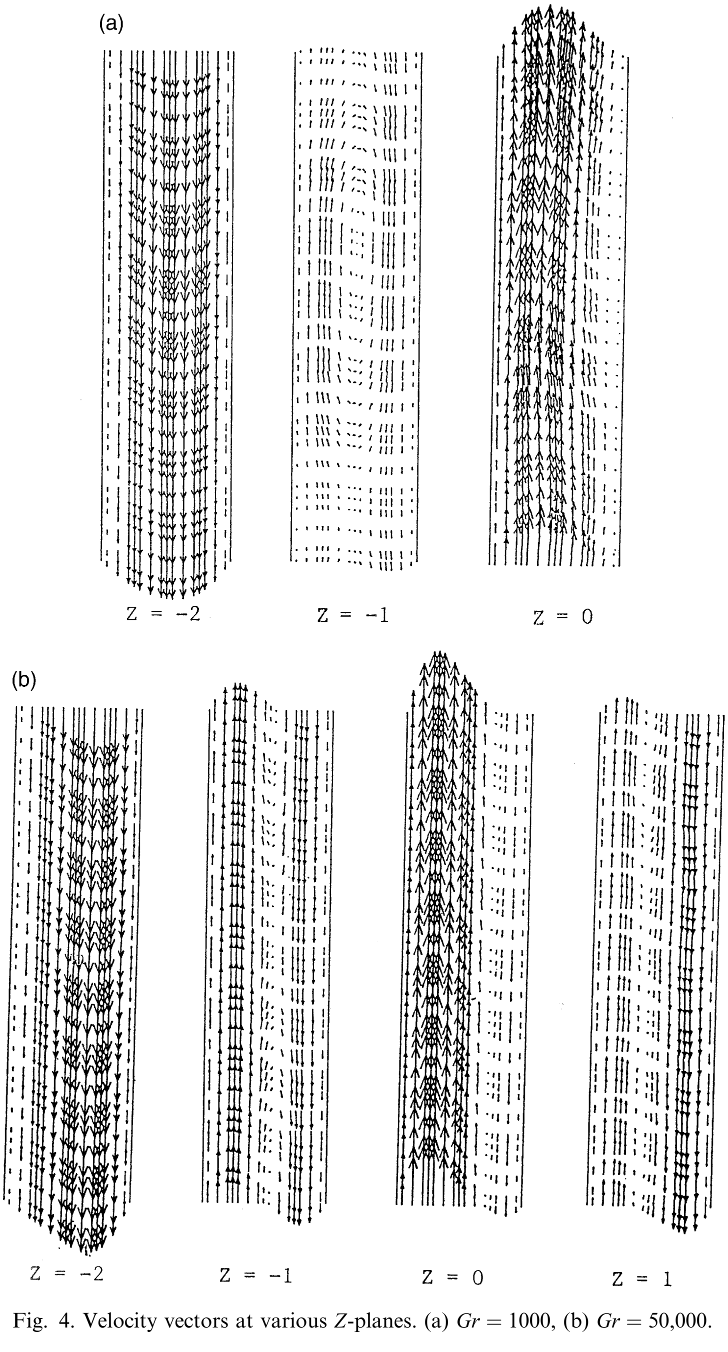

Fig. 4. Velocity vectors at various Z-planes. (a) $Gr = 1000$, (b) $Gr = 50{,}000$.

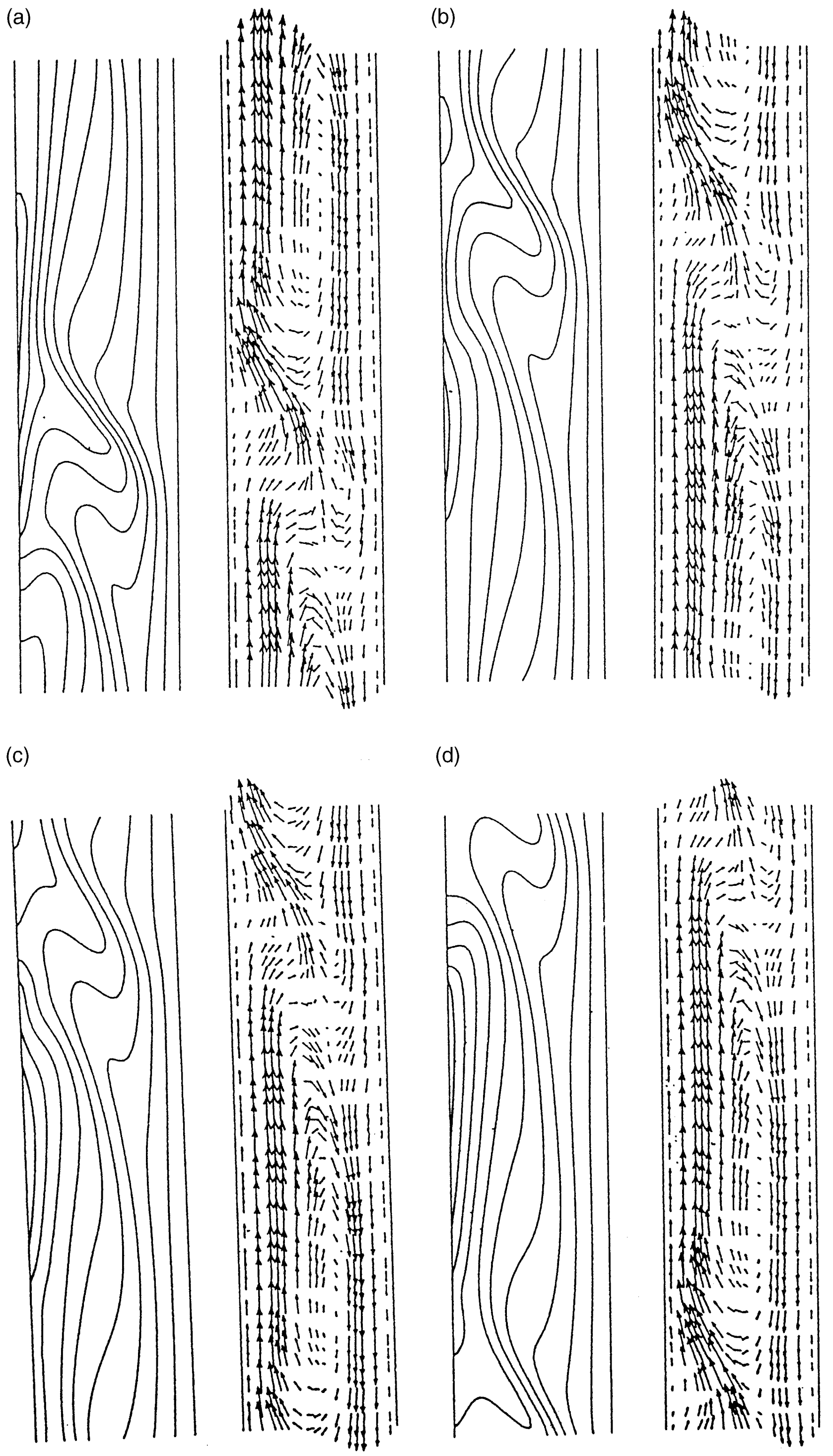

Fig. 5. Instantaneous velocity vectors and isotherms at $Z = -1$, $Gr = 50{,}000$. (a) $3T/10$, (b) $8T/10$, (c) $9T/10$, (d) T.

$N = 7$ have also been obtained. The difference between solutions with $N = 5$ and solutions with $N = 7$ is <2%.

Computations were performed on a Stardent P3000 superworkstation and an IBM RS/6000 model 950.

4. Results

Examination of the governing equations (1)–(5) and boundary conditions, Eqs. (8)–(12b), reveals that for fixed geometry the convective flow is governed by the Prandtl number, *Pr*, Rayleigh number, *Ra* (or equivalently, Grashof number, $Gr = Ra/Pr$), and the dimensionless channel reference temperature, $\Theta_b^* = kT_b/(q''l)$. Additional independent dimensionless parameters describe the domain geometry of the problem. In this paper, *Pr* is set to 0.71 (for air), the dimensionless channel reference temperature is maintained at $\Theta_b^* = 0.12$, *Gr* ranges from 0.1 to 5×10^4. For all numerical simulations the aspect ratios are $A_y = 4$, $A_z = 4$, $A_{cy} = 2$, $A_{cz} = 2$, $A_{sy} = 2$, and $A_{sz} = 2$.

4.1. Analytical solution

To assess the accuracy of the numerical procedure, a 3-D analytical solution, valid in the limit of small values of Grashof number, has been derived. Considering regular small parameter expansions of the form,

$$\vec{V} = Gr\,\vec{V}_1(X,Y,Z) + Gr^2\,\vec{V}_2(X,Y,Z) + \cdots \tag{13}$$

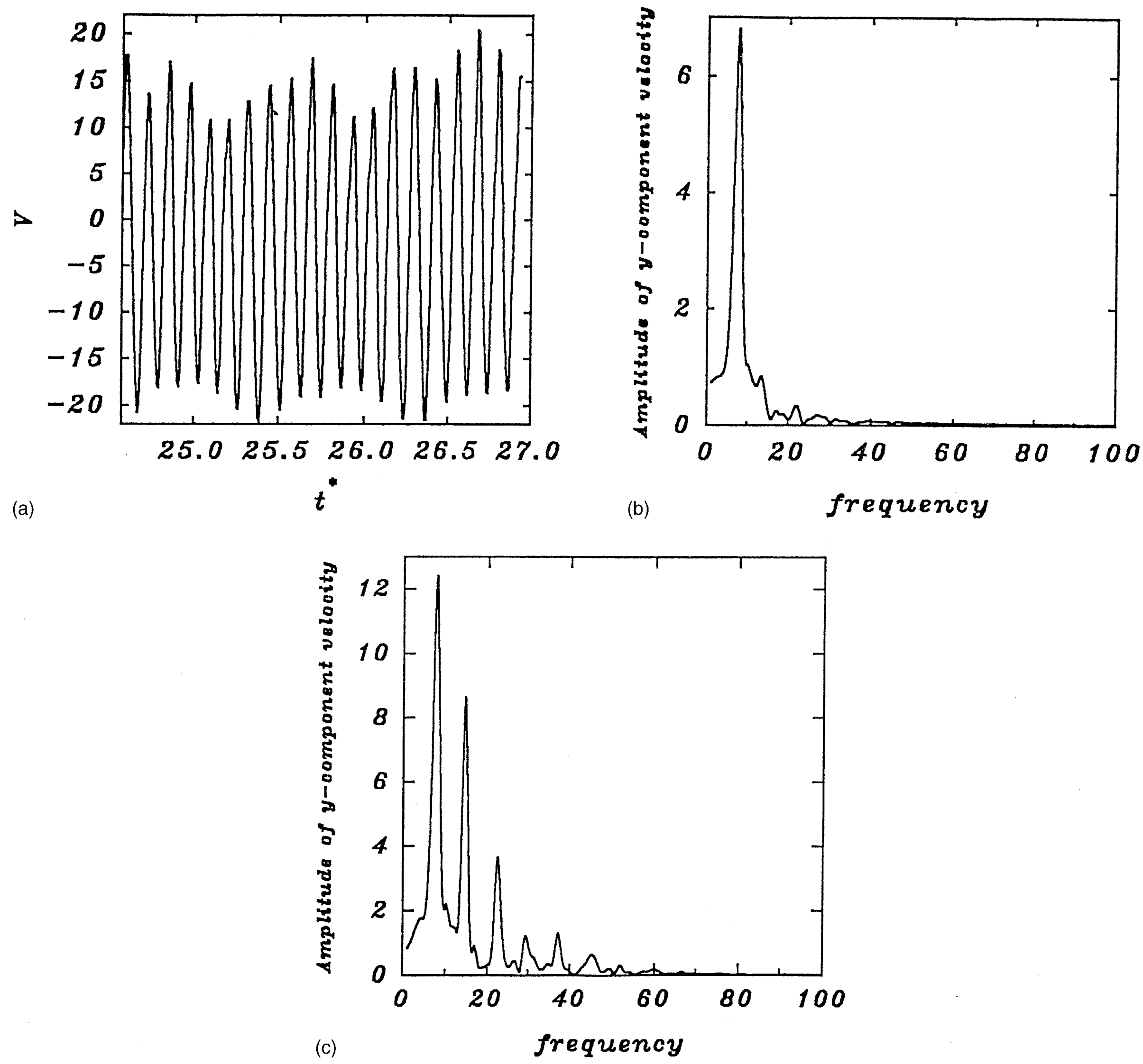

Fig. 6. (a) Time record of vertical velocity component at (0.79, 1.09, −0.5), $Gr = 50{,}000$. (b) Frequency content of the vertical velocity component at (0.79, 1.09, −0.5), $Gr = 50{,}000$. (c) Frequency content of the vertical velocity component at (0.207, −0.25, −1.0), $Gr = 50{,}000$.

$$\Theta = \Theta_0(X,Y,Z) + Gr\,\Theta_1(X,Y,Z) + \cdots \tag{14}$$

$$P = Gr P_1(X,Y,Z) + Gr^2 P_2(X,Y,Z) + \cdots \tag{15}$$

for the steady velocity, temperature and pressure fields respectively and substituting Eqs. (13)–(15) into Eqs. (1)–(5) we obtain,

$$\frac{\partial U_1}{\partial X} + \frac{\partial V_1}{\partial Y} + \frac{\partial W_1}{\partial Z} = 0, \tag{16}$$

$$\nabla^2 U_1 = \frac{1}{Pr}\frac{\partial P_1}{\partial X}, \tag{17}$$

$$\nabla^2 V_1 = \frac{1}{Pr}\frac{\partial P_1}{\partial Y} - Pr\,\Theta_0, \tag{18}$$

$$\nabla^2 W_1 = \frac{1}{Pr}\frac{\partial P_1}{\partial Z}, \tag{19}$$

$$\nabla^2 \Theta_0 = 0. \tag{20}$$

Considering Eqs. (17)–(19) and making use of Eq. (16), the governing equation for P_1 can be written as,

$$\nabla^2 P_1 = Pr^2 \frac{\partial \Theta_0}{\partial Y}. \tag{21}$$

By applying the Laplacian operator, ∇^2, on both sides of Eq. (17) and making use of Eq. (21) one obtains

$$\nabla^4 U_1 = Pr \frac{\partial^2 \Theta_0}{\partial Y\,\partial X}. \tag{22}$$

Eqs. (13)–(15) imply that the boundary conditions given by Eqs. (8)–(12b) are applicable to U_1, V_1, W_1 and Θ_0. Note that to complete the formulation of the problem, we need to impose an additional boundary condition on U_1 as it is governed by a biharmonic equation, Eq. (22). Taking into account that $\vec{V}_1$ satisfies the no-slip conditions at the walls and using Eq. (16) we obtain

$$\frac{\partial U_1}{\partial X} = 0 \quad \text{on all solid walls.} \tag{23}$$

Eqs. (16)–(20) with boundary conditions, Eqs. (8)–(12b) and (23) describe a set of boundary value problems which determine uniquely the functions Θ_0, U_1, V_1, W_1 and P_1. The solution can be written in the form

$$\Theta_0 = \sum_{j=0}^{\infty}\sum_{k=0}^{\infty} b_{jk}(X)\cos\lambda_j Y \cos\gamma_k Z, \tag{24}$$

$$V_1 = \sum_{j=0}^{\infty}\sum_{k=0}^{\infty} a_{jk}(X)\cos\lambda_j Y \cos\gamma_k Z, \tag{25}$$

$$U_1 = \sum_{j=1}^{\infty}\sum_{k=0}^{\infty} c_{jk}(X)\sin\lambda_j Y \cos\gamma_k Z, \tag{26}$$

$$W_1 = \sum_{j=1}^{\infty}\sum_{k=1}^{\infty} G_{jk}(X)\sin\lambda_j Y \sin\gamma_k Z, \tag{27}$$

$$P_1 = \sum_{j=1}^{\infty}\sum_{k=0}^{\infty} F_{jk}(X)\sin\lambda_j Y \cos\gamma_k Z, \tag{28}$$

where $\lambda_j = 2\pi j/A_y$ and $\gamma_k = 2\pi k/A_z$. The detailed procedure of obtaining the above solution can be found in Gunes [19]. The expressions for $a_{jk}(X)$, $b_{jk}(X)$, $c_{jk}(X)$, $F_{jk}(X)$ and $G_{jk}(X)$ in terms of hyperbolic functions and polynomials are given in Appendix A.

- Based on the above solution, the leading order approximation to the volume flow rate through the channel is

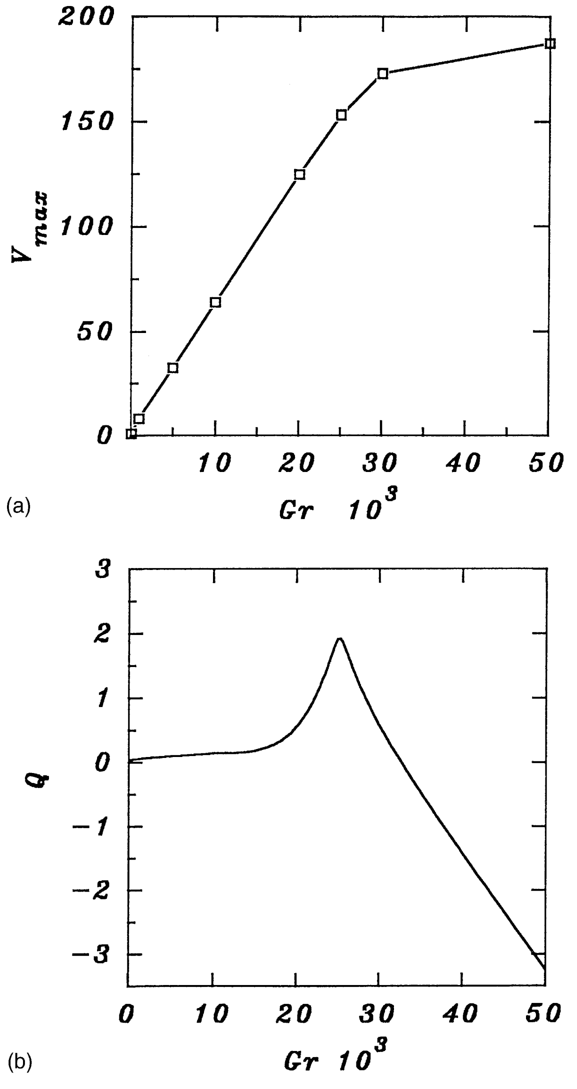

Fig. 7. (a) Variation of dimensionless maximum velocity with *Gr*. (b) Variation of dimensionless net volume flow rate with *Gr*.

$$Q = \frac{A_z Gr Pr}{24}\left\{\frac{A_{cy}A_{cz}}{A_y A_z} - 2\Theta_b^*\right\}. \tag{29}$$

- The Nusselt number at the left (hot) wall, based on the wall temperature, can be expressed as

$$Nu_l(Y,Z) = \frac{1}{\Theta_0(0,Y,Z)}, \tag{30}$$

while the average Nusselt number, $\overline{Nu}_C$, for the chip (heat source) can be calculated as,

$$\overline{Nu}_C = \frac{1}{A_{cy}A_{cz}}\int_{-A_{cz}/2}^{A_{cz}/2}\int_{-A_{cy}/2}^{A_{cy}/2} Nu_l(Y,Z)\,\mathrm{d}Y\,\mathrm{d}Z. \tag{31}$$

- At the right vertical isothermal wall, the Nusselt number

$$Nu(Y,Z) = -\frac{\partial\Theta}{\partial X}(1,Y,Z) \tag{32}$$

can be expressed as

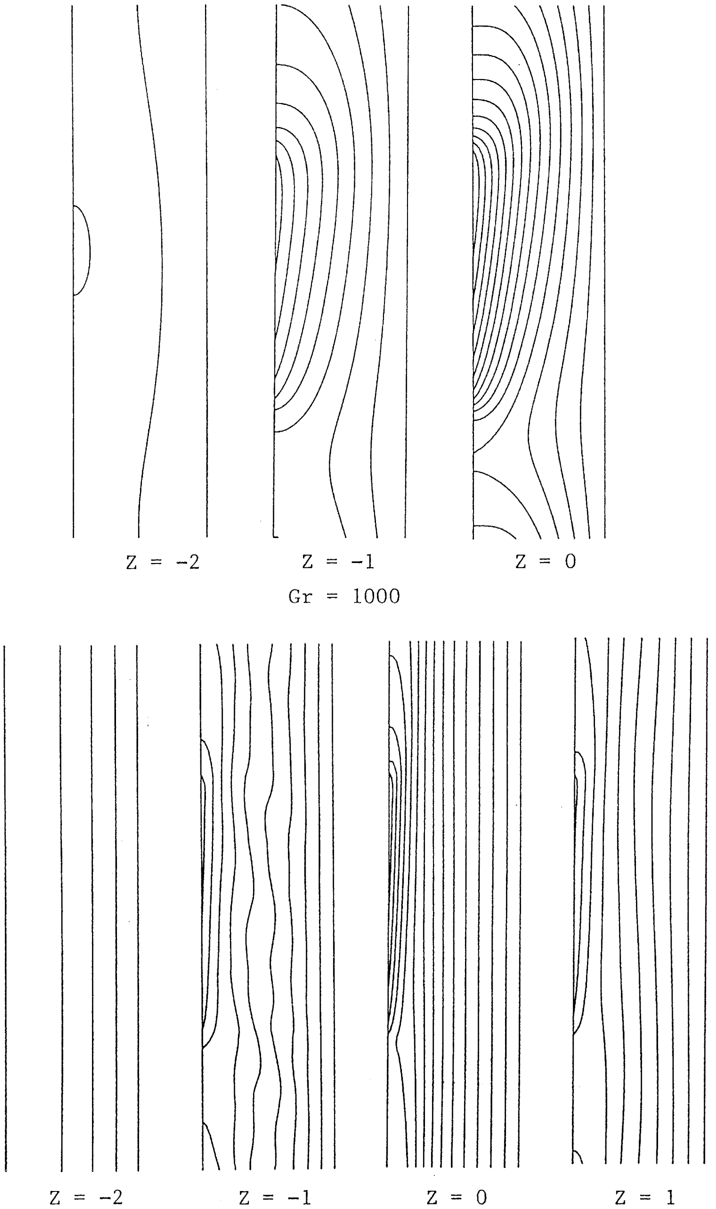

Fig. 8. Isotherms at various Z-planes ($\Theta_b^* = 0.12$ and $Pr = 0.71$).

$$Nu(Y,Z) = -\sum_{j=0}^{\infty}\sum_{k=0}^{\infty} g_{jk}\cos\lambda_j Y\cos\gamma_k Z, \tag{33}$$

where

$$g_{00} = -\frac{A_{cy}A_{cz}}{A_yA_z}, \quad g_{j0} = k_j\lambda_j, \quad g_{0k} = m_k\gamma_k,$$

$$g_{jk} = n_{jk}\rho_{jk}, \tag{34}$$

where k_j, m_k, n_{jk} and ρ_{jk} are given in Appendix A.

4.2. Computer program validation

The analytical solution presented above is compared with our numerical solutions for a range of Grashof numbers. The comparison of the field variables is carried out for $A_{cy} = A_{cz} = 2$, $A_y = A_z = 4$, $Pr = 0.71$ and dimensionless channel reference temperature $\Theta_b^* = 0.125$. For $Gr \to 0$, the numerical results are in excellent agreement with the analytical solution. However, at

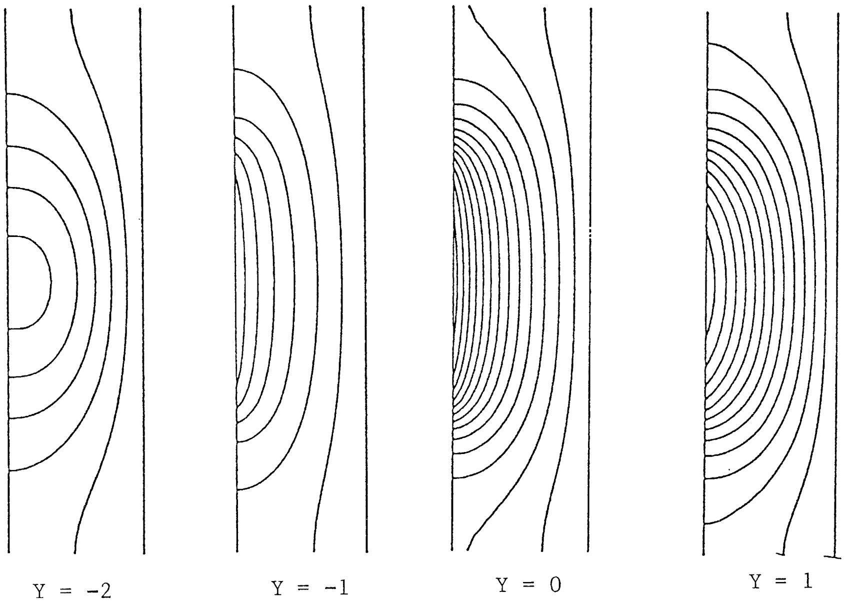

Gr = 1000

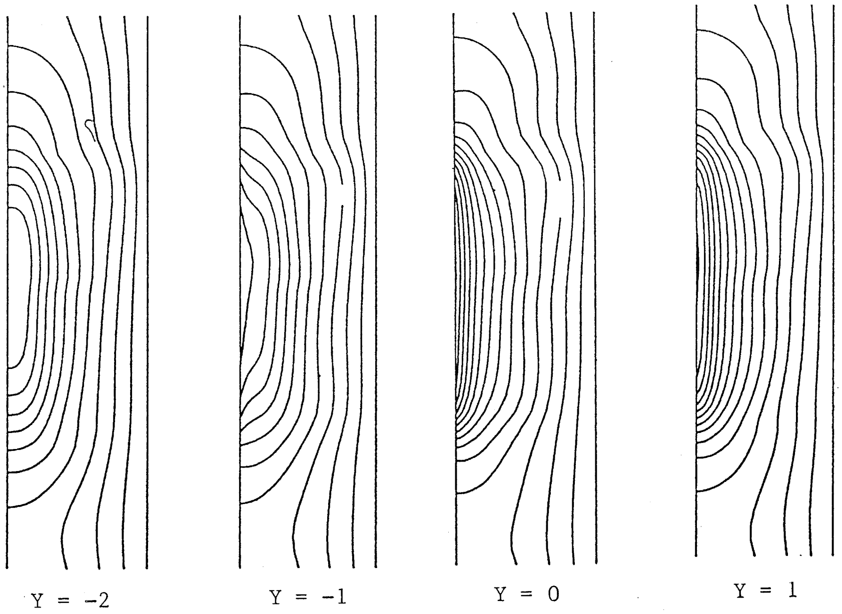

Gr = 50000

Fig. 9. Isotherms at various Y-planes.

large values of *Gr*, discrepancies are very pronounced due to the breakdown of the analytical solution. Table 1 gives the maximum values of temperature and vertical velocity for various values of Grashof number. As seen from Table 1, the relative error between the numerical and analytical values is within 1% for $Gr \leqslant 200$. In addition, numerical and analytical values of the field variables were compared at each grid point for selected vertical Z-planes at $Gr = 1$ and 100. At $Gr = 1$, the comparison revealed that the relative error is 0.1–0.5%, being close to 1.0% at very few points. However, for $Gr = 100$ the accuracy depends strongly on the constant Z-planes. At $Z = -2$ plane, the relative error in temperature at each grid point is about 1–3%. However, close to the middle plane, e.g. at $Z = 0.17$, the local error increases to as high as 10%. For the Y-component of velocity, the local error is in the range of 1–4% at $Z = -2$, increasing to about 1–7% close to the mid-vertical plane. The reason for this behavior of the relative error distribution will be apparent after the discussion of the solution behavior obtained numerically at moderate and high values of Grashof number.

Table 2 summarizes the comparison of numerical and analytical solutions for the velocity components in X and Z directions. In addition, pressure values are compared in Table 3. The Nusselt number distributions obtained analytically and numerically are in excellent agreement for $Gr \leqslant 10^2$. Further analytical solutions and the effects of heat source aspect ratios on flow and thermal fields are presented in [19].

4.3. Numerical solutions

Numerical solutions are obtained by gradually increasing the value of Grashof number. All simulations performed are time accurate. If a steady (time-independent) solution exists it is found as the steady-state solution of Eqs. (1)–(5) after all transients die out, i.e. in the limit $t \to \infty$. Time-independent steady-state solutions have been found for $Gr < Gr^* \simeq 28{,}000$. These solutions are symmetric about the mid-vertical plane ($Z = 0$). At $Gr = 28,000$ and $\Theta_b^* = 0.12$ the solutions becomes spontaneously periodic in time. All solutions obtained for $Gr > Gr^*$ and $\Theta_b^* = 0.12$ are oscillatory in time exhibiting temporal patterns of increasing complexity as *Gr* increases. The onset of temporal instability is accompanied by a breakdown of the symmetry of the fields about $Z = 0$ that is characteristic of all time-independent solutions.

4.3.1. Flow characteristics

The flow field is fully 3-D at all values of *Gr* and is characterized by strong net upward flow in the channel segment in front of the heat sources ($-1 \leqslant Z \leqslant 1$) and downward flow in the channel segment in front of the adiabatic wall ($1 \leqslant Z \leqslant 2$ and $-2 \leqslant Z \leqslant -1$). Fig. 3 depicts the contours of constant V (vertical velocity component) at the mid horizontal plane ($Y = 0$) for $Gr = 10^3$, 3×10^4 and 5×10^4. The pattern depicted in Fig. 3 does not change significantly at other elevations, $Y =$ const. However, the velocity field depends strongly on the Z and X coordinates as can be seen in Fig. 4, which shows the velocity vectors at various Z-planes. As *Gr* increases, the location of the maximum velocity at $Z = -2$ plane moves closer to the cold wall. On the other hand, at $Z = 0$ (mid-vertical plane) the maximum velocity moves closer to the hot wall while very small velocities are observed near the cold wall. In Figs. 3 and 4, time-averaged values are depicted for $Gr = 3 \times 10^4$ and 5×10^4. Instantaneous vector fields and corresponding isotherms are presented in Fig. 5. At $Gr = 5 \times 10^4$, a rather strong vortex, which is convected upward in the

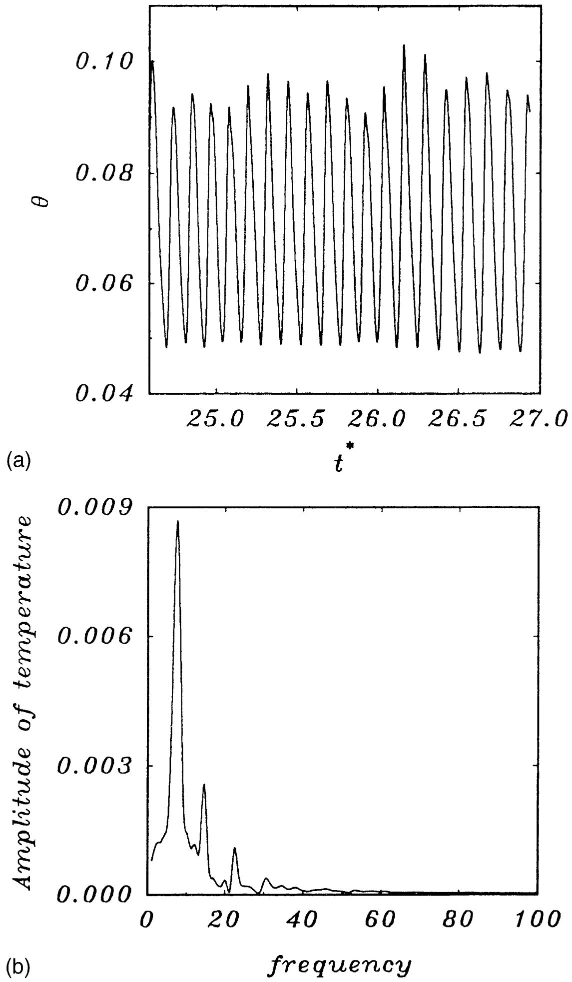

Fig. 10. (a) Time record of temperature at (0.79, 1.09, −0.5), $Gr = 50{,}000$. (b) Frequency content of temperature at (0.79, 1.09, −0.5), $Gr = 50{,}000$.

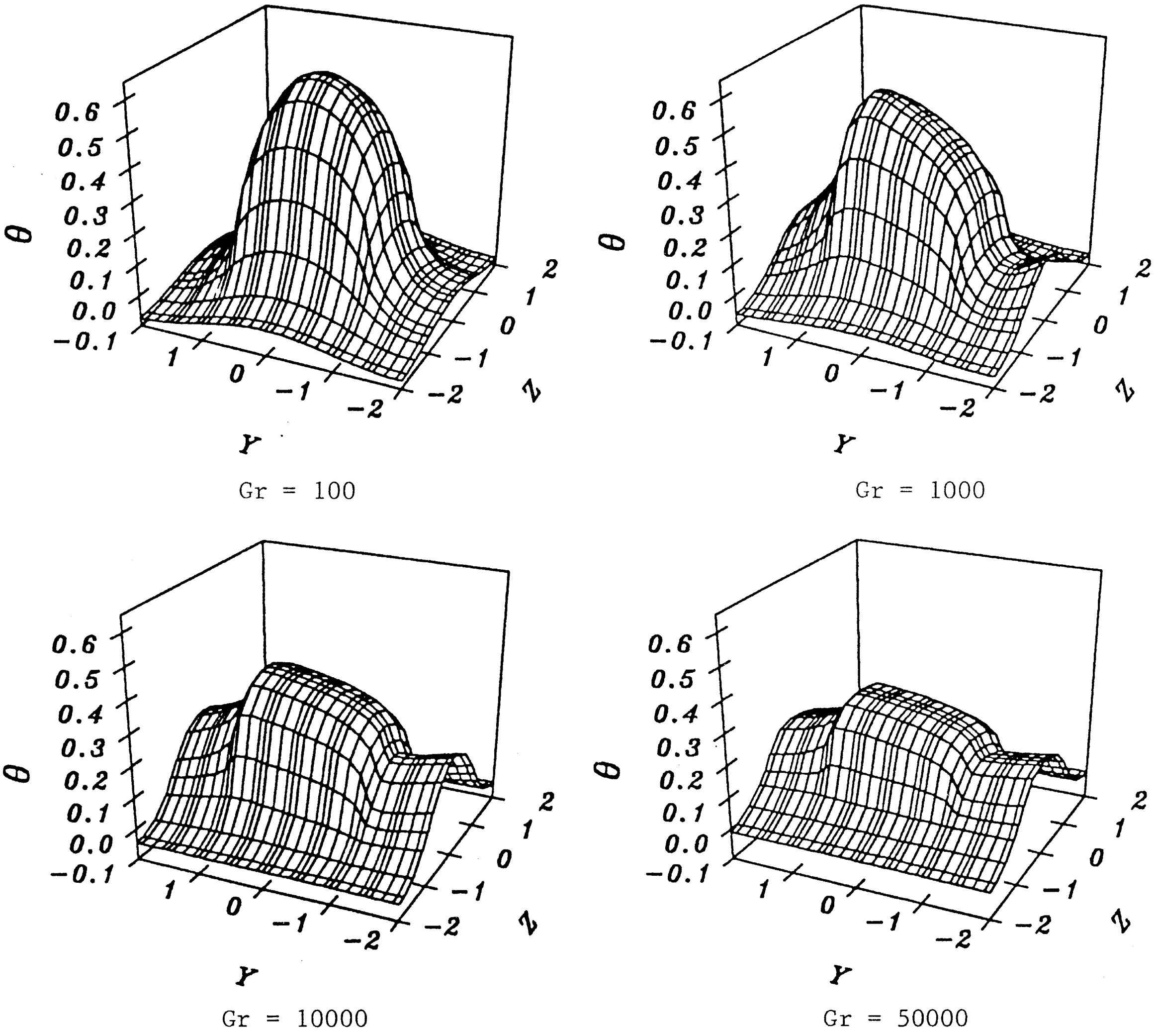

Fig. 11. Temperature distribution on the left vertical wall ($X = 0$).

channel, is observable at $Z = -1$ plane. Fig. 6a shows the time record of the vertical velocity component at $X = 0.79$, $Y = 1.09$, and $Z = -0.5$ for $Gr = 5 \times 10^4$ while Fig. 6b shows the frequency content on this signal obtained by fast Fourier transform (FFT). It should be noted that this frequency spectrum is not representative of all points in the channel. For example, at point ($X = 0.207$, $Y = -0.25$, $Z = -1.00$) time oscillations are more vigorous and include several frequencies as illustrated in Fig. 6c. Fig. 7a shows the maximum dimensionless velocity over the whole computational domain. It increases linearly with Gr for sufficiently small values of Gr ($Gr \leqslant 10^3$—conduction dominated regime). For higher values of Gr the slope of $V_{\max}$ changes as convection effects become important. Finally, the time-averaged $V_{\max}$ exhibits a further change in slope at about $Gr \simeq Gr^*$ where the solution becomes time dependent. Fig. 7b shows the dependence of induced net volume flow rate on Gr.

4.3.2. Heat transfer characteristics

Heat transfer characteristics are fully three-dimensional for all values of Gr. At $Gr = 10^2$, the temperature field is practically that of pure conduction. As Gr increases, beginning with $Gr = 10^3$ convective effects become important (Fig. 8). At $Gr = 10^4$, isotherms become almost straight vertical lines at $Z = -2$ and at $Z = 0$ boundary layers start forming in the vicinity of the heat sources. Temperatures at $Z = 0$ depend only on X in most of the channel width as the boundary layers become increasingly thin as Gr increases. Similar characteristics are exhibited by velocities at $Z = -2$ and 0 planes. Fig. 9 shows the isotherms at various Y-planes for selected Gr. Again, the symmetry breakdown for $Gr \geqslant Gr^*$ is observable in the temperature field as velocity and temperature fields are coupled. A typical record of temperature oscillations and its frequency decomposition are shown in Fig. 10a and b for a point located at $X = 0.79$, $Y = 1.09$, $Z = -0.5$, and $Gr = 5 \times 10^4$.

The variation of dimensionless temperature at the heated wall ($X = 0$) is shown in Fig. 11. In the conduction solution, the temperature distribution is symmetric about the Y and Z axes and the maximum and minimum temperatures occur at $Y = 0$ and ± 2, respectively. At $Gr = 10^3$, the locations of maximum and minimum temperature are moved to $Y = 0.68$ and -1.44, and are shifted to $Y = 0.84$ and -1.16, respectively, at $Gr = 10^4$. However, for higher values of Gr, the locations of the extrema of the temperature field remain fairly constant. On the other hand, as expected, the difference $\Theta_{\max} - \Theta_{\min}$ at the heated wall ($X = 0$) decreases with increasing Gr (Fig. 11). Similar trend is obtained for the maximum dimensionless temperature as seen in Fig. 12. For small Gr ($Gr \leqslant 10^3$), the maximum dimensionless temperature decreases linearly with Gr, giving rise to a 12% drop in its value at $Gr = 10^3$. As natural convection cooling becomes appreciable, a 35% drop is observed at $Gr = 10^4$. For $Gr = 5 \times 10^4$ the averaged-in-time maximum dimensionless temperature is 47% lower than the value corresponding to the conduction solution.

Fig. 13 shows the local Nusselt number along the heat source (chip) surface defined as

$$Nu_{\mathrm{C}}(Y, Z, t^*) = \frac{q'' l}{k(T - T_{\mathrm{b}})} \tag{35}$$

or in terms of the dimensionless temperature

$$Nu_{\mathrm{C}} = \frac{1}{\Theta(X = 0, Y, Z, t^*)}, \tag{36}$$

for various values of Gr. The average chip Nusselt number, defined in Eq. (31), is shown in Fig. 14. Note that for both local and average chip Nusselt numbers, averaged-in-time values are reported for $Gr > Gr^*$. As can be seen in Fig. 14, $\overline{Nu}_{\mathrm{C}}$ is practically constant for $Gr \leqslant 100$, i.e, the temperature field can essentially be characterized by the conduction solution. Between $100 < Gr < 3 \times 10^3$ a transition occurs and from this point on a linear increase in $\overline{Nu}_{\mathrm{C}}$ is observed up to $Gr = Gr^*$, where the solution becomes oscillatory in time.

The Nusselt number distribution at the right (cold) wall, defined in Eq. (32), is shown in Fig. 15 for various values of Gr. It should be noted that for the time-dependent cases, the instantaneous Nusselt number distributions at the right wall can be very different from the averaged-in-time distributions shown in Fig. 15. For example, Fig. 16 shows two typical instantaneous distributions of $Nu(X = 1, Y, Z, t^*)$ at $Gr = 3 \times 10^4$ and 5×10^4 that reflect the strong time-dependent character of the temperature field which of course is directly coupled to the velocity fluctuations.

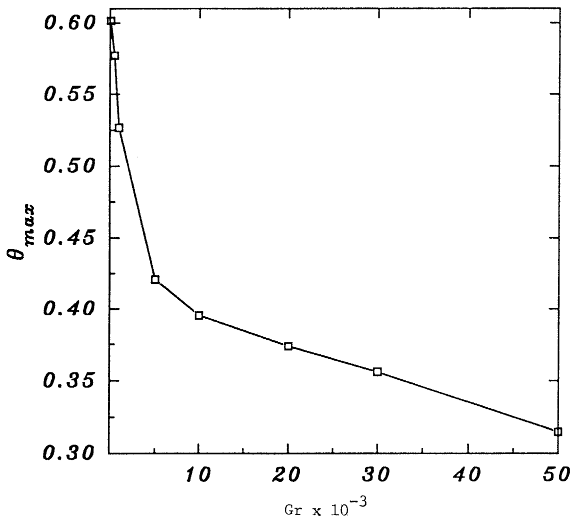

Fig. 12. Variation of maximum dimensionless temperature with Gr.

5. Summary

We have presented a study of three-dimensional free convection of a Boussinesq fluid with $Pr = 0.71$ in a vertical channel. The flow is driven by heat sources flush mounted on the left vertical channel wall and periodically arranged in both horizontal and vertical directions. A three-dimensional analytical solution, valid in the limit of small values of Grashof number was also presented and compared with the solutions obtained numerically. The agreement was excellent for sufficiently small Gr. Emphasis was given on the self-sustained oscillations that spontaneously appear at sufficiently large values of Grashof number. In the present work, the net volume flowrate through the channel is small. Flow and thermal fields as well as the values of critical Grashof number are vastly different when the background temperature is varied considerably.

We have shown that direct numerical simulation is a promising approach for studying convective instabilities in the presence of doubly periodic thermal boundary conditions. However, the parameter space for the problem considered is very large and an exhaustive numerical investigation of the influence of all geometric

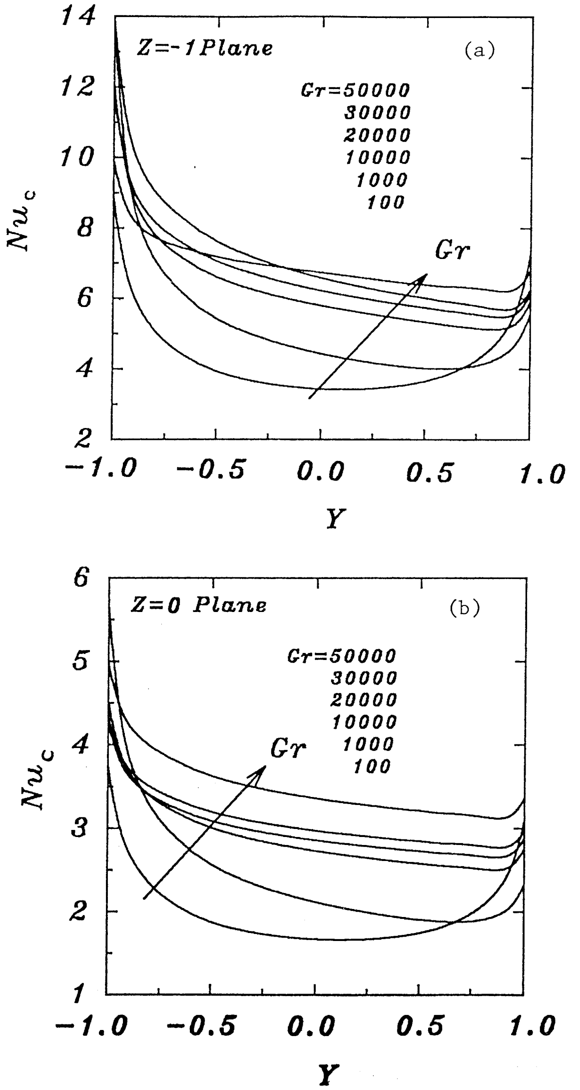

Fig. 13. Local chip Nusselt number variation for various values of *Gr*. (a) $Z=-1$, (b) $Z=0$.

and thermal parameters depends on further advances in computing capabilities.

Appendix A

In this appendix we summarize the expressions for the expansion coefficients (functions of X) appearing in Eqs. (24)–(28).

(a) Dimensionless temperature:

$$b_{00}(X) = \frac{A_{cy}A_{cz}}{A_yA_z}(1-X) - \Theta_b^*, \tag{A.1}$$

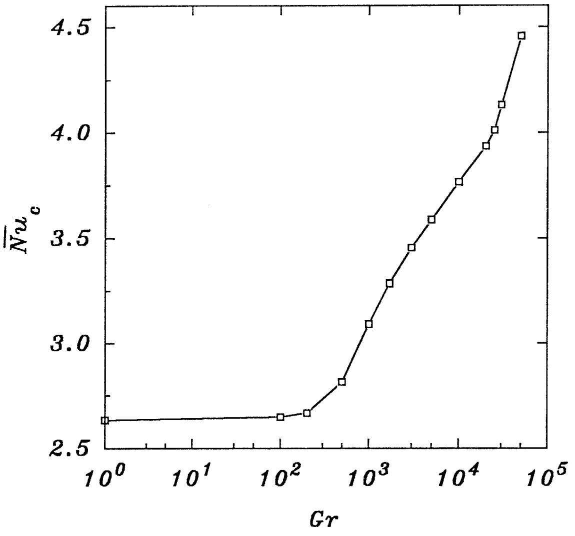

Fig. 14. Variation of average chip Nusselt number with *Gr*.

$$b_{j0}(X) = k_j \sinh\lambda_j(X-1)$$
$$\text{where } k_j = \frac{-4A_{cz}\sin\left(\frac{A_{cy}}{2}\lambda_j\right)}{\lambda_j^2A_yA_z\cosh\lambda_j}, \tag{A.2}$$

$$b_{0k}(X) = m_k \sinh\gamma_k(X-1)$$
$$\text{where } m_k = \frac{-4A_{cy}\sin\left(\frac{A_{cz}}{2}\gamma_k\right)}{\gamma_k^2A_yA_z\cosh\gamma_k}, \tag{A.3}$$

$$b_{jk}(X) = n_{jk} \sinh\rho_{jk}(X-1)$$
$$\text{where } n_{jk} = \frac{-16\sin\left(\frac{A_{cz}}{2}\lambda_j\right)\sin\left(\frac{A_{cy}}{2}\gamma_k\right)}{\lambda_j\gamma_k\rho_{jk}A_yA_z\cosh\rho_{jk}} \tag{A.4}$$

and

$$\rho_{jk} = \sqrt{\lambda_j^2+\gamma_k^2}. \tag{A.5}$$

(b) Dimensionless x-velocity component:

$$\begin{aligned} c_{jk}(X) &= E_1(\sinh\rho_{jk}X - \rho_{jk}X\cosh\rho_{jk}X) \\ &\quad + E_3X\sinh\rho_{jk}X - \frac{Pr\,n_{jk}\lambda_j}{8\rho_{jk}}X^2 \\ &\quad \times \cosh\rho_{jk}(X-1), \end{aligned} \tag{A.6}$$

where

$$E_1 = \frac{K_{jk}}{8\rho_{jk}^2}\left\{\frac{\rho_{jk}\cosh\rho_{jk} - \sinh\rho_{jk}}{\rho_{jk}^2 - \sinh^2\rho_{jk}}\right\}, \tag{A.7a}$$

$$E_3 = \frac{K_{jk}}{8\rho_{jk}^2}\left\{\frac{(\rho_{jk}^2+2)\sinh\rho_{jk} - 2\rho_{jk}\cosh\rho_{jk}}{\rho_{jk}^2 - \sinh^2\rho_{jk}}\right\}, \tag{A.7b}$$

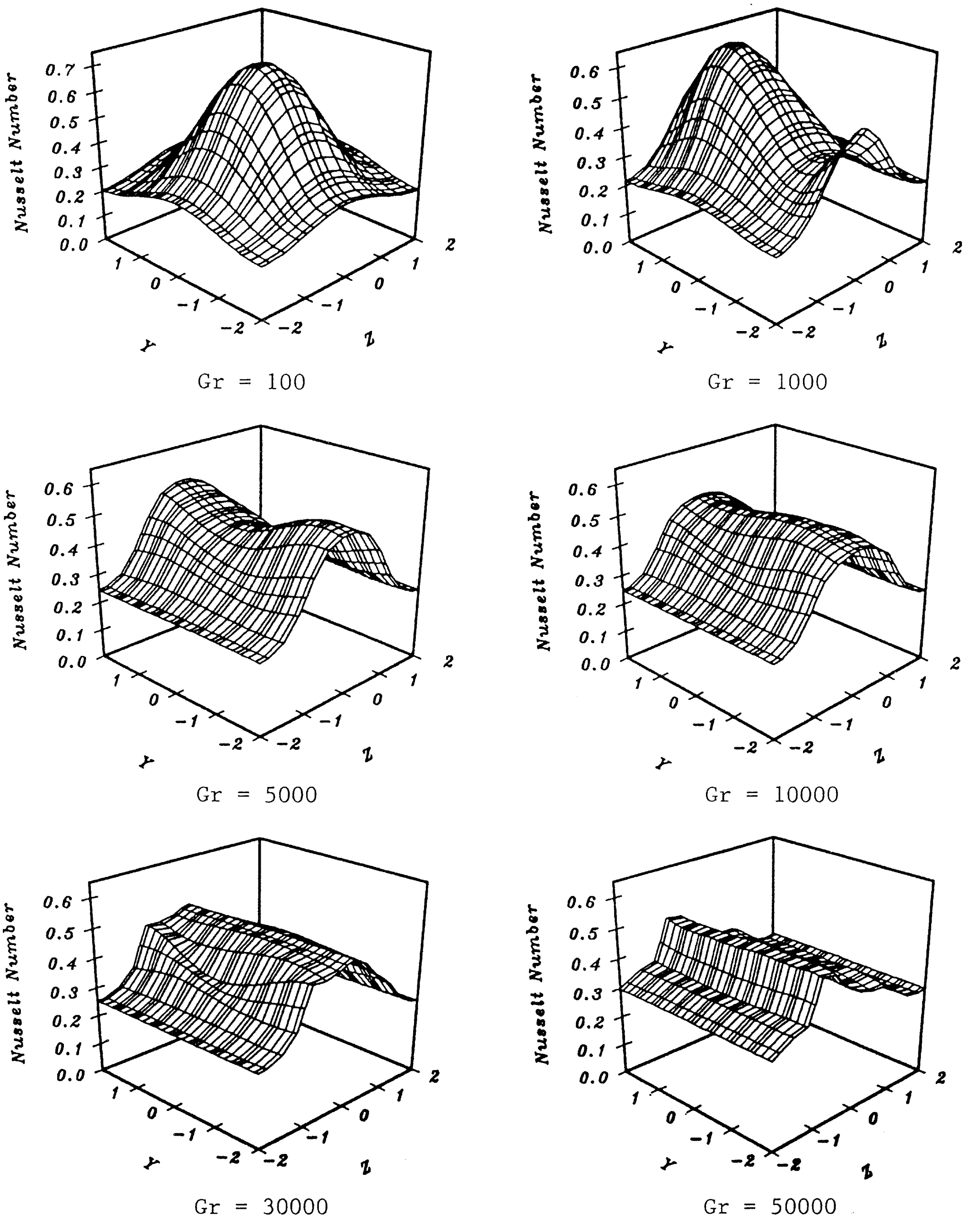

Gr = 100 Gr = 1000

Gr = 5000 Gr = 10000

Gr = 30000 Gr = 50000

Fig. 15. Nusselt number distribution at the right vertical wall ($X = 1$).

$$K_{jk} = -Pr\, n_{jk} \rho_{jk} \lambda_j \tag{A.8a}$$

and n_{jk} and ρ_{jk} are as defined in Eqs. (A.4) and (A.5), respectively. $c_{j0}(X)$ is given by Eq. (A.6) with $\gamma_k = 0$ ($k = 0$), or $\lambda_j = \rho_{jk}$ and

$$K_{j0} = -Pr\, k_j \lambda_j^2, \tag{A.8b}$$

where k_j is given in Eq. (A.2).

(c) Dimensionless pressure:

$$\begin{aligned} F_{jk}(X) &= 2(E_3 \sinh \rho_{jk} X - E_1 \rho_{jk} \cosh \rho_{jk} X) \\ &\quad + \frac{K_{jk}}{2\rho_{jk}} \left\{ X \cosh \rho_{jk}(X-1) \right. \\ &\quad \left. - \frac{1}{2\rho_{jk}} \sinh \rho_{jk}(X-1) \right\}, \end{aligned} \tag{A.9}$$

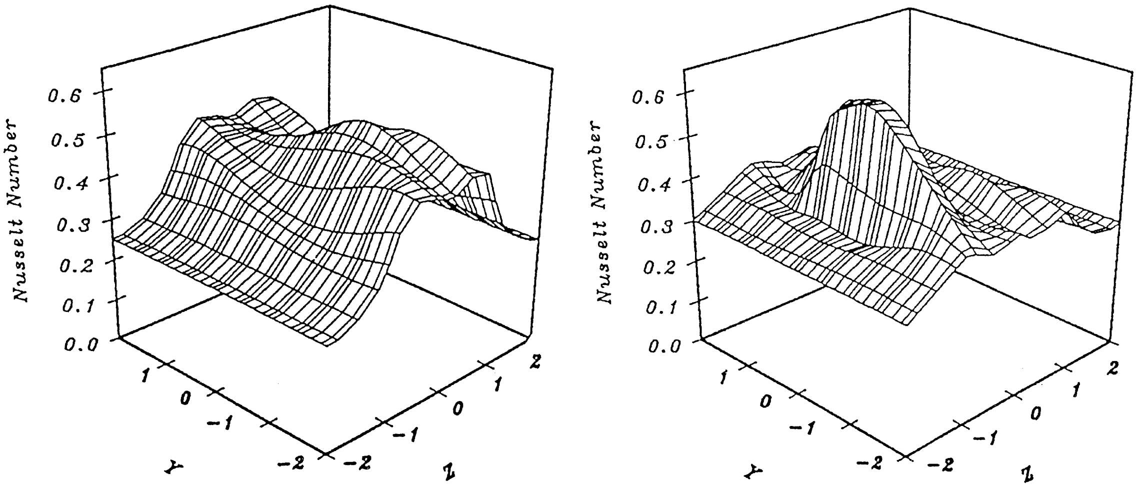

Gr = 30000 Gr = 50000

Fig. 16. Instantaneous Nusselt number distributions at the right vertical wall.

where E_1, E_3 and K_{jk} are given in Eqs. (A.7a)–(A.8a), respectively.

Substituting $\gamma_k = 0$, or $\lambda_j = \rho_{jk}$ as discussed before, $F_{j0}(X)$ can be written in the form of Eq. (A.9).

(d) Dimensionless z-velocity component:

$$G_{jk}(X) = \sinh\rho_{jk}X(A_1 + \gamma_k E_1 X) - \frac{E_3\gamma_k}{\rho_{jk}}X\cosh\rho_{jk}X + \frac{\gamma_k K_{jk}}{4\rho_{jk}^4}X\left\{\cosh\lambda_j(X-1) - \frac{1}{2}\rho_{jk}X\sinh\lambda_j(X-1)\right\}, \tag{A.10}$$

where

$$A_1 = \gamma_k\left(\frac{E_3}{\rho_{jk}}\coth\rho_{jk} - E_1 - \frac{K_{jk}}{4\rho_{jk}^4\sinh\rho_{jk}}\right), \tag{A.11}$$

and E_1, E_2 and K_{jk} are given in Eqs. (A.7a)–(A.8a), respectively.

(e) Dimensionless y-velocity component:

$$e_{00}(X) = Pr\,X(X-1)\left\{\frac{A_{cy}A_{cz}}{6A_yA_z}(X-2) + \frac{1}{2}\Theta_b^*\right\}, \tag{A.12}$$

$$e_{j0}(X) = \sinh\lambda_jX(A - \lambda_jE_{10}X) + E_{30}X\cosh\lambda_jX - \frac{Pr\,k_j}{4}\left\{\frac{1}{2}X^2\sinh\lambda_j(X-1) + \frac{X}{\lambda_j}\cosh\lambda_j(X-1)\right\}, \tag{A.13}$$

where

$$A = \frac{Pr\,k_j}{2\lambda_j}\left\{\frac{1}{\sinh\lambda_j} - \frac{1}{2}\right\} + \lambda_jE_1 - E_3\coth\lambda_j, \tag{A.14}$$

$$E_{10} = \frac{K_{j0}}{8\lambda_j^2}\left\{\frac{\lambda_j\cosh\lambda_j - \sinh\lambda_j}{\lambda_j^2 - \sinh^2\lambda_j}\right\}, \tag{A.15a}$$

$$E_{30} = \frac{K_{j0}}{8\lambda_j^2}\left\{\frac{(\lambda_j^2+2)\sinh\lambda_j - 2\lambda_j\cosh\lambda_j}{\lambda_j^2 - \sinh^2\lambda_j}\right\} \tag{A.15b}$$

and k_j and K_{j0} are given in Eqs. (A.2) and (A.8b), respectively.

$$e_{0k}(X) = \frac{Pr\,m_k}{2\gamma_k}\left\{\frac{\sinh\gamma_kX}{\sinh\gamma_k} - X\cosh\gamma_k(X-1)\right\}, \tag{A.16}$$

where m_k is given by Eq. (A.3).

$$e_{jk}(X) = \sinh\rho_{jk}X(H_1 - \lambda_jE_1X) + \frac{\lambda_j}{\rho_{jk}}E_3X\cosh\rho_{jk}X - \frac{\lambda_jK_{jk}}{8\rho_{jk}^3}X^2(\sinh\rho_{jk}(X-1)) - \left(\frac{Pr\,n_{jk}X}{2\rho_{jk}} + \frac{\lambda_jK_{jk}X}{4\rho_{jk}^4}\right)\cosh\rho_{jk}(X-1), \tag{A.17}$$

where

$$H_1 = \frac{Pr\,n_{jk}}{2\rho_{jk}\sinh\rho_{jk}} + \lambda_j\left(E_1 - \frac{E_3}{\rho_{jk}}\coth\rho_{jk}\right) + \frac{\lambda_jK_{jk}}{4\rho_{jk}^4}. \tag{A.18}$$

References

[1] T.J. Heindel, F.P. Incropera, S. Ramadyani, Enhancement of natural convection heat transfer from an array of discrete heat sources, Int. J. Heat Mass Transfer 39 (1996) 479–490.

[2] G.P. Peterson, A. Ortega, Thermal control of electronic equipment and devices, Adv. Heat Transfer 20 (1990) 181–314.

[3] F.P. Incropera, Convection heat transfer in electronic equipment cooling, J. Heat Transfer 110 (1988) 1097–1111.

[4] M.S. Bohn, R. Anderson, Temperature and heat flux distribution in a natural convection enclosure flow, J. Heat Transfer 108 (1986) 471–475.

[5] A. Liakopoulos, P.A. Blythe, P.G. Simpkins, in: A.F. Emery (Ed.), Convective flows in tall cavities, Simulation and Numerical Methods in Heat Transfer, HTD-Vol. 157, ASME, 1990, pp. 81–87.

[6] X. Huang, A. Liakopoulos, Convective flow and heat transfer in tall enclosures with flush-mounted heat sources, Advances in Electronic Packaging, vol. EEP-4-2, ASME, 1993, pp. 769–778.

[7] M. Keyhani, V. Prasad, R. Cox, An experimental study of natural convection in a vertical cavity with discrete heat sources, J. Heat Transfer 110 (1988) 616–624.

[8] K.A. Park, A.E. Bergles, Natural convection heat transfer characteristics of simulated microelectronic chips, J. Heat Transfer 109 (1987) 90–96.

[9] Y. Joshi, D.L. Knight, Natural convection from a column of flush heat sources in a vertical channel in water, J. Electronic Packaging 112 (1990) 367–374.

[10] D. Kuhn, P.H. Oosthuizen, Three-dimensional transient natural convective flow in a rectangular enclosure with localized heating, Natural Convection in Enclosures, vol. HTD-63, ASME, 1986, pp. 55–62.

[11] I. Sezai, A.A. Mohamad, Natural convection from a discrete heat source on the bottom of a horizontal enclosure, Int. J. Heat Mass Transfer 43 (2000) 2257–2266.

[12] K.-T. Lee, Laminar natural convection heat and mass transfer in vertical rectangular ducts, Int. J. Heat Mass Transfer 42 (1999) 4523–4534.

[13] H. Gunes, A. Liakopoulos, Three-dimensional buoyancy-driven flow in a vertical channel with heated ribs, The Twelfth Int. Symp. Transport Phenomena, Istanbul, Turkey, July 16–20, 2000, pp. 149–154.

[14] A.T. Patera, A spectral element method for fluid dynamics: laminar flow in a channel expansion, J. Comp. Phys. 54 (1984) 468–488.

[15] G.E. Karniadakis, Spectral element simulations of laminar and turbulent flows in complex geometries, Appl. Numer. Math. 6 (1–2) (1989) 85–105.

[16] G. Becker, P. Carnevali, B. Chayapathy, W. Imaino, R.B. Morris, Y. Tsuji, B. Yendler, Singularities in p-type finite element computations: numerical experiments on the locality of pollution effects, J. Appl. Mech. 58 (1991) 586–588.

[17] NEKTON Users Manual, Release 2.9, Nektonics Inc., 1994.

[18] N.N. Yanenko, The Method of Fractional Steps for Solving Multi-Dimensional Problems, Springer, 1971.

[19] H. Gunes, Analytical solutions of thermal convection problems with spatially periodic boundary conditions, Heat Mass Transfer, in press.